RSC Advances

ROYAL SOCIETY OF CHEMISTRY

www.rsc.org/advances

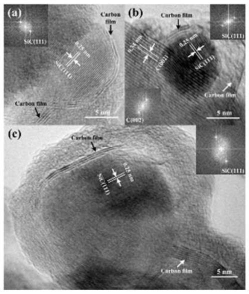

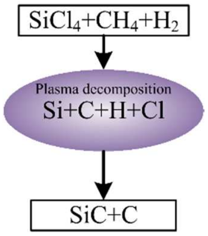

SiC nanocrystal was fabricated at high rate with $SiCl_4$ as Si source by thermal plasma enhanced chemical vapor deposition through the assembly of precursor atoms.

SiC nanocrystal: high rate deposition and nano-scale control by thermal plasma

Tengfei Cao, Haibao Zhang, Binhang Yan, Wei Lu, Yi Cheng [*]
Department of Chemical Engineering, Tsinghua University, Beijing, China.
E-mail: yicheng@tsinghua.edu.cn; Fax: +86-10-62772051; Tel: +86-10-62794468

Abstract

This work applied thermal plasma to enhance the deposition process of SiC nanocrystals with $SiCl_4$ and CH_4 as Si source and C source, respectively. Thin films containing SiC nanocrystals, a-Si and graphite are deposited on the substrates. The morphology and crystalline structure of the samples were characterized by SEM, TEM, XRD, etc. SiC nanocrystals were observed being covered by carbon films and embedded in the network formed by graphite and a-Si. The effect of $SiCl_4$ input rate on deposition process and product properties has been studied in detail combining the characterization and optical emission spectroscopy (OES) diagnostic results. Based on the OES diagnostic of the plasma zone, the concentrations of atomic Si and C in the gas phase are justified to be the main factors affecting the deposition process. Finally, a simple deposition mechanism is deduced depending on the experimental results, which indicates the formation of SiC nanocrystals through the assembly of atomic species in the plasma.

Introduction

Silicon carbide (SiC) is a well-known wide-bandgap semiconductor for excellent thermal, mechanical and electrical properties, such as high thermal conductivity, high thermal resistance, high breakdown voltage, high electron saturation velocity and chemical inertness.[1, 2] It has been the material of choice for high voltage and high current devices operated at elevated temperatures.[3, 4] It is also biocompatible with blood and can be utilized as the coating material of artificial joint.[5] Large-area, high-quality single crystal SiC substrates are nowadays available due to the development in crystal growth. In recent years, the discovery of new forms of SiC, such as superlattices and nanocrystals has been triggered by nano-technology. The SiC nanocrystals have several superior properties in comparison with bulk SiC materials. Among them, the photoluminescence (PL) property of SiC nanocrystals have been paid close attention to and widely studied.[6-10] Combined with its biocompatible property, SiC nanocrystals are applied in *in vivo* biological imaging as biomarkers which requires the production of SiC nanocrystals in a relatively large amount.[11-14]

SiC nanocrystal is conventionally produced by chemical etching or plasma enhanced chemical vapor deposition (PECVD) method. The fabrication of SiC nanocrystals using electrochemical anodization method has been reported since 1990s.[6, 7, 15] This method involves corrosive solutions and the fabrication process is relatively slow, which makes it difficult to be handled at industrial scale. Wet chemical etching, replacing the electrochemical anodization method, has become the major method for SiC nanocrystal fabrication presently.[9, 10, 16, 17] The prepared nanocrystals have the features of small diameters and narrow size distribution. It is acknowledged that the wet chemical etching process is simple and can be easily conducted in the lab. However, this process also involves corrosive solutions which may lead to sewage pollution when applied on a large scale. PECVD is a relatively cleaner process widely applied for the synthesis of nano-materials.[18-20] To be noted, PECVD is the most commonly used technique for the production of cubic SiC (3C-SiC, also β-SiC) while also applied for SiC nanocrystal fabrication during the past decade.[21-28] In general, SiH_4 and hydrocarbons were used as silicon and carbon source gas, respectively,[21-23] while organosilane was used as single source for both Si and C[27]. Both radio-frequency (RF) plasma[21, 22] and electron cyclotron resonance (ECR) plasma[23] could be adopted in PECVD processes. Moreover, SiC nanocrystal can also be deposited by reactive plasma sputtering of bulk Si and C or SiC targets.[24-26, 28] However, these cold plasma enhanced CVD processes all have low deposition rates, which makes it difficult to fabricate SiC nanocrystal on a large scale and thus hampers the industrial application of SiC nanocrystal.

Thermal plasma intensification has been adopted in high-rate CVD of nanocrystalline silicon (nc-Si) getting a deposition rate of 9.78 nm s^{-1}.[29] Compared to cold plasma, thermal plasma offers higher temperature and higher reactive species density, thus offers much higher fluxes of energy and matter in nanomaterial fabrication.[30, 31] Chaudhry et al.[22] has utilized a 15 kW thermal plasma to fabricate polycrystalline SiC and studied the influence of deposition temperature. However, the analysis of thermal plasma deposition process and product properties is scarce. In this work, SiC nanocrystal was fabricated using an atmospheric pressure thermal plasma enhanced CVD (APTPECVD) process and the effect of raw material input rate on deposition process and product properties was studied. The inductively coupled plasma (ICP) was adopted, which is particularly appropriate for high-purity product synthesis due to the absence of electrode.

We chose $SiCl_4$ instead of SiH_4 or organosilane as the Si source. SiH_4 is a hazardous material because of its pyrophoricity in air,[32] while $SiCl_4$ is chemically more stable, which is liquid at room temperature. Most of $SiCl_4$ comes from the polycrystalline silicon fabrication process using SIMENS method in photovoltaic industry as the by-product. About 10~15 t high-purity $SiCl_4$ is produced when producing 1 t polycrystalline silicon. This leads to the much lower price of $SiCl_4$ than most organosilane and the very large amount of $SiCl_4$ storage, which makes $SiCl_4$ a cheap, abundant and thus more appropriate Si source for thermal plasma process in comparison with SiH_4 and organosilane. To our knowledge, this is the first time that $SiCl_4$ is reported to be used as Si source for SiC nanocrystal fabrication through a PECVD process. Furthermore, optical emission spectroscopy (OES) diagnostic was carried out during the thermal plasma enhanced CVD process to analyze the gas phase composition in plasma zone and better understand the plasma deposition process.[33]

Results and discussion

Samples were deposited on both crystalline silicon (c-Si) and glass substrates. X-ray diffraction (XRD) patterns of samples at different $SiCl_4$ input rates are shown in Fig. 1. Diffraction peaks at 35.414°, 41.231°, 59.879° and 71.610° correspond with (111), (200), (220) and (311) crystal planes of β-SiC. Broadened peaks at 25.782° and 68.545° correspond with (002) plane of graphite and (400) plane of c-Si, respectively. Silicon is in amorphous phase according to the diffraction peak structure observed. Therefore, SiC nanocrystals are embedded in a mixture of graphite and a-Si. Diffraction peak at 29.396° corresponding with (111) plane of c-Si was observed at very low $SiCl_4$ input rate, i.e., 0.11 mol h^{-1}, while the intensities of diffraction peaks of β-SiC are relatively low. So the sample mainly composes a-Si and graphite at very low $SiCl_4$ input rate. However, the intensities of diffraction peaks of (111), (220) and (311) crystal planes of SiC enhance with the increase of $SiCl_4$ input rate. The diffraction peak of (200) crystal plane of SiC becomes notable when $SiCl_4$ input rate gets higher than 0.32 mol h^{-1}. The broadening of the diffraction peaks is due to the anisotropic shape of the crystallites, while the relatively large width of the peaks indicates the presence of very small SiC grain diameters.[28] The average diameters of

SiC grain at different $SiCl_4$ input rate were calculated using Scherrer's formula,

$$d_{\mathrm{XRD}} = \frac{0.9\lambda}{\beta\cos\theta} \qquad (1)$$

where λ is the X-ray beam wavelength (λ=1.54056 Å in this work), β is the broadening of the X-ray diffraction line expressed in radian.[34] The average grain diameters were calculated to be in the range of 21-33 nm and summarized in Table 1.

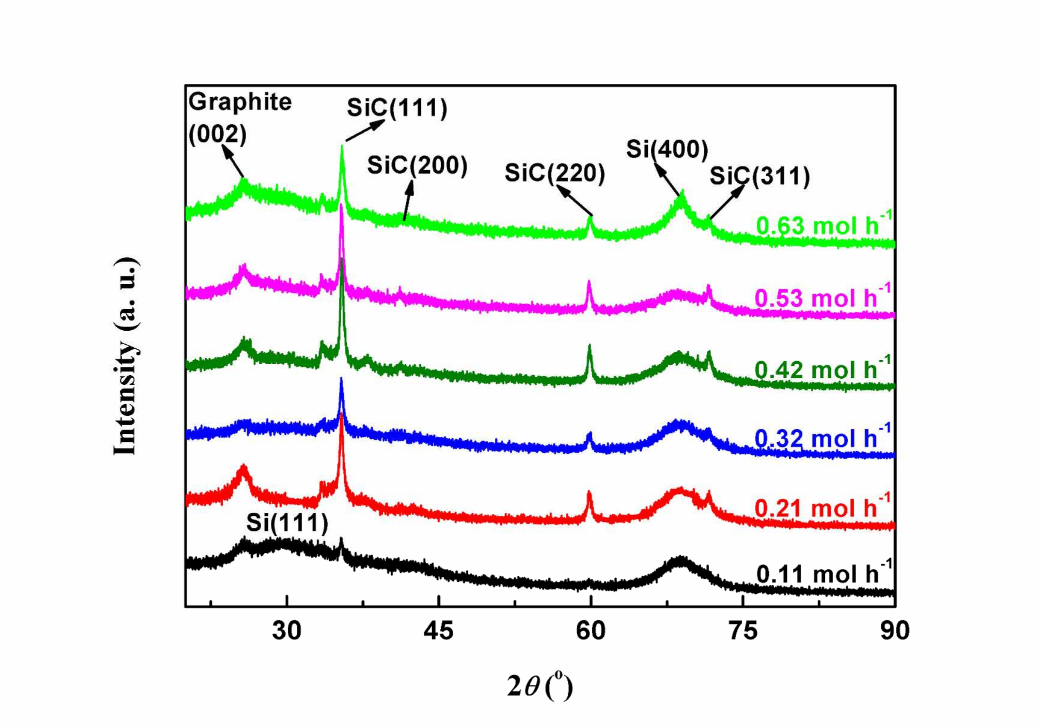

Fig. 1 XRD patterns of samples deposited at different $SiCl_4$ input rate.

Table 1 SiC grain diameters of samples at different $SiCl_4$ input rate calculated using Scherrer's formula.

$SiCl_4$ input rate (mol h^{-1})	Grain diameter (nm)
0.11	33
0.21	24
0.32	24

0.42	29
0.53	32
0.63	21

The results of Raman spectrum analysis agree well with XRD characterization. The typical Raman spectrum of the sample deposited at $SiCl_4$ input rate of 0.53 mol h^{-1} is given in Fig. 2(a). The broad peak centered around 480 cm^{-1} originates from a-Si.[35] The peaks at ~1,350 cm^{-1}, ~1,580 cm^{-1} and ~2,690 cm^{-1} correspond with the D band, G band and 2D band of graphite, respectively.[36, 37] The intensities of D band and 2D band peaks are relatively high, which indicates the existence of defect in the graphite structure.[38] Therefore, the composition of the thin film can be determined to be SiC nanocrystals, a-Si and graphite basing on XRD and Raman spectra analysis results. The intensities of D band and G band both decrease with increasing $SiCl_4$ input rate as shown in Fig. 2(b). This may result from the decrease of the amount of graphite in the product with increasing $SiCl_4$ input rate. The intensity ratio of D band to G band improves with increasing $SiCl_4$ input rate which means the amount of disordered structures in graphite improves with increasing $SiCl_4$ input rate.[36] The effect of $SiCl_4$ input rate on product composition and properties will be further analyzed and discussed later.

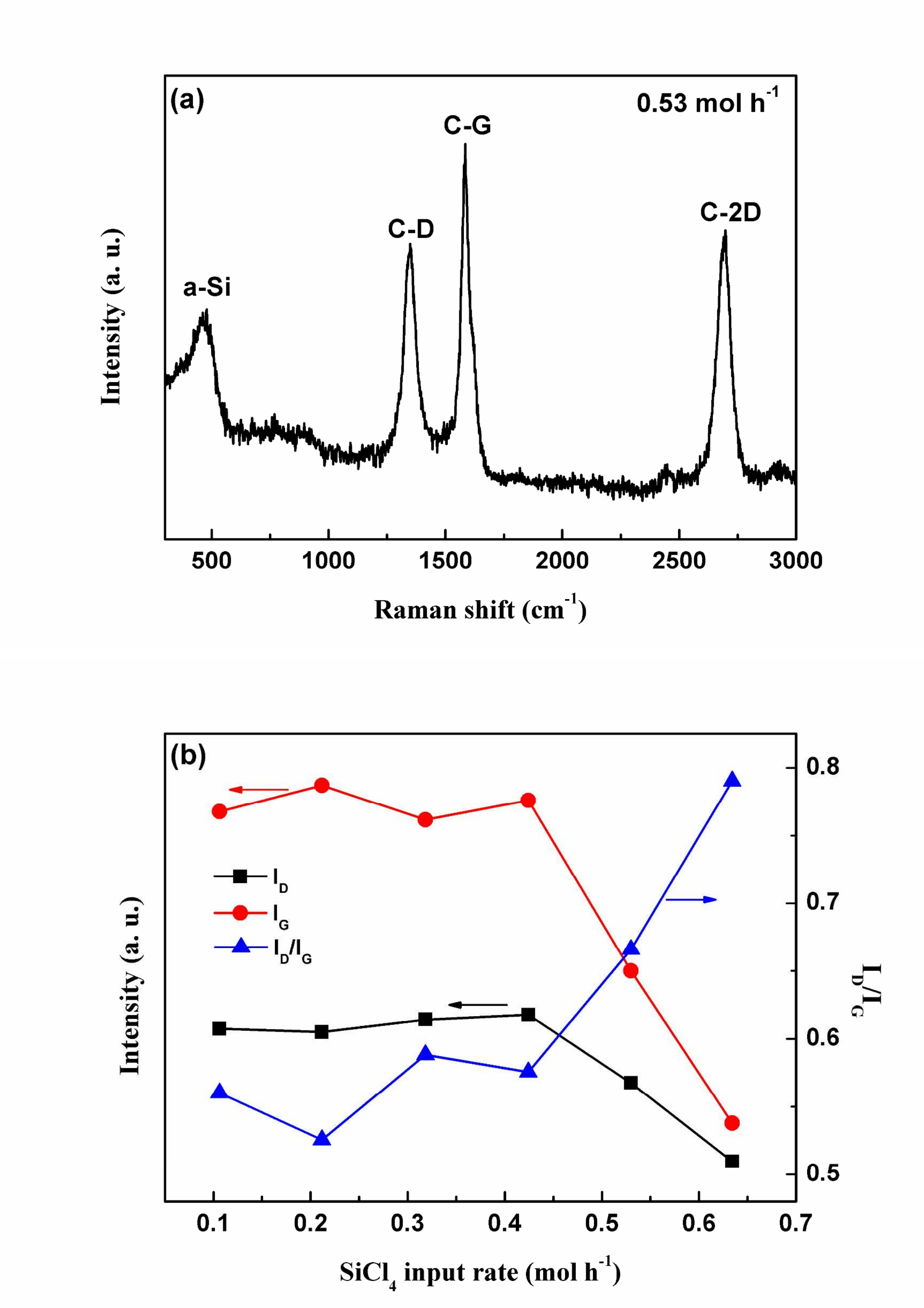

Fig. 2 (a) Typical Raman spectrum of sample at $SiCl_4$ input rate of 0.53 mol h^{-1}; (b) Effect of $SiCl_4$ input rate on intensities of D band, G band and the intensity ratio of D band to G band.

The samples have porous structures as shown in the scanning electron microscope (SEM) images in Fig. 3. This porous structure consists of nano-sized spheres and branched networks. All samples have similar network structures while the diameters of the spheres change with $SiCl_4$ input rate. Film thickness was determined basing on the cross-sectional SEM images of the samples as shown in Fig. 3(e). The deposition rates of the thin films were calculated with that film thickness analyzed by SEM. The effect of $SiCl_4$ input rate on deposition rate is given in Fig. 4. The deposition rate improves with increasing $SiCl_4$ input rate. This deposition rate with thermal plasma enhancement reaches a maximum of ~70 nm s^{-1}, which is relatively high compared with that of cold plasma processes[19].

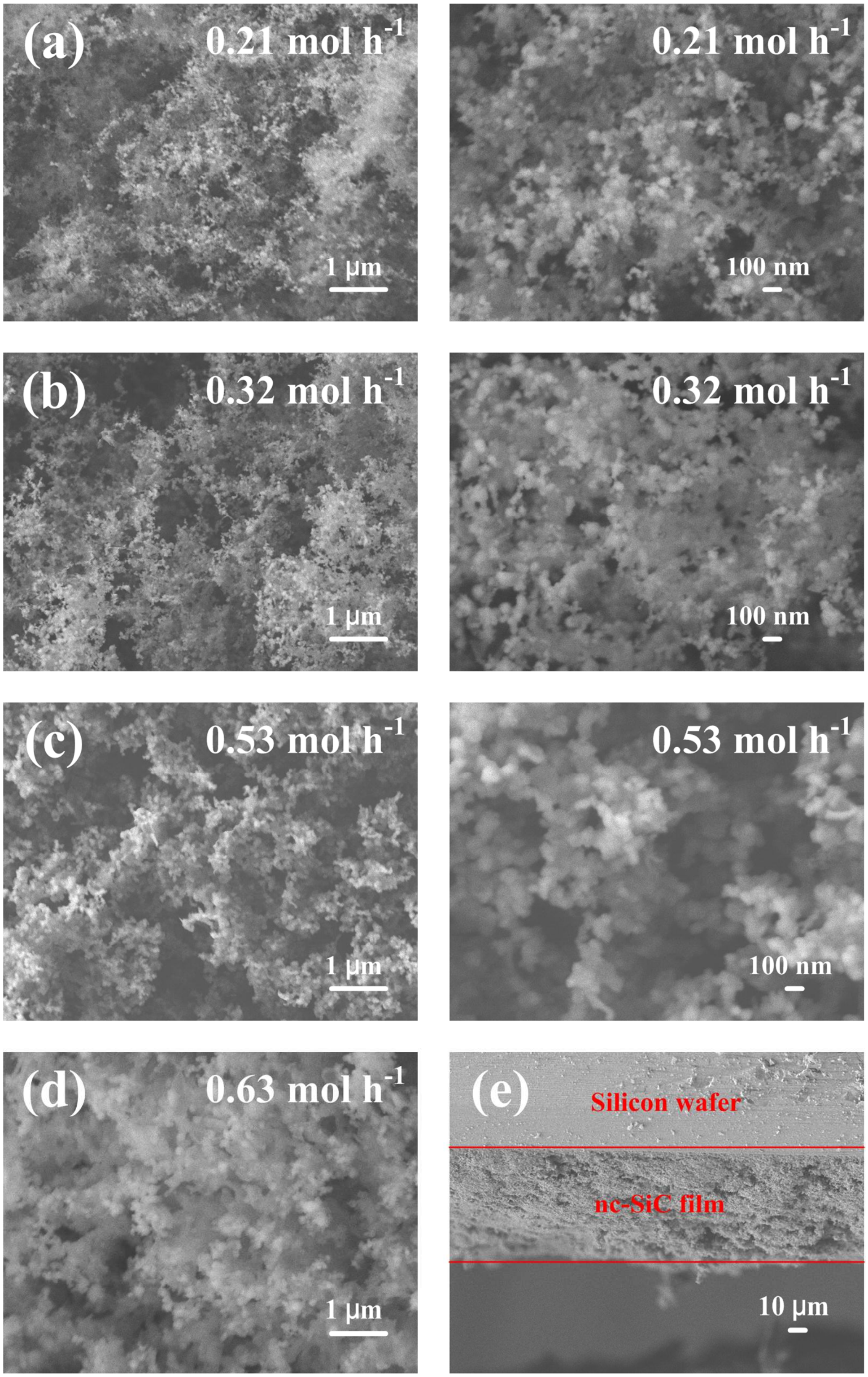

Fig. 3 SEM images of samples at $SiCl_4$ input rate of (a) 0.21 mol h^{-1}, (b) 0.32 mol h^{-1}, (c) 0.53 mol h^{-1} and (d) 0.63 mol h^{-1}; (e) A typical cross-sectional SEM image of the sample at $SiCl_4$ input rate

of 0.42 mol h^{-1}.

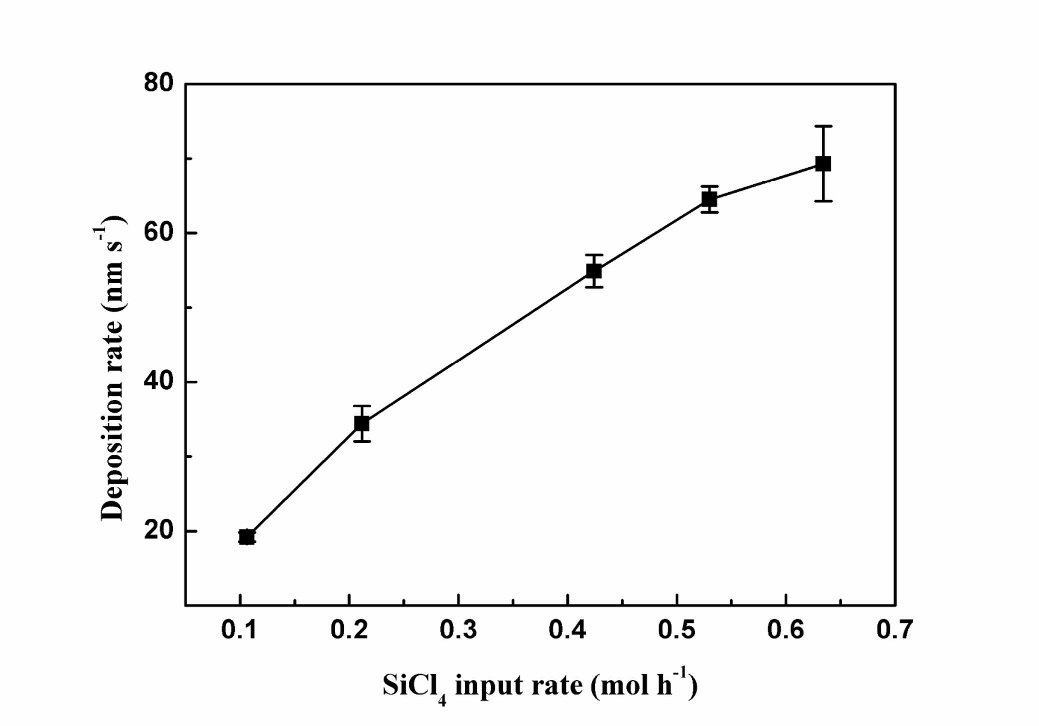

Fig. 4 Effect of $SiCl_4$ input rate on thin film deposition rate.

Transmission electron microscope (TEM) characterization was carried out to further investigate the morphology of the samples. Fig. 5 shows the typical TEM images of samples at different $SiCl_4$ input rate. SiC nanocrystals and graphite indicated by XRD and Raman spectra analysis are observed and marked in the images. SiC nanocrystals are formed with the covering of carbon film and embedded in a network consisting of a-Si and graphite. The diameter of SiC nanocrystal is in the range from less than 10 nm to larger than 30 nm. The carbon film covering SiC nanocrystal consists 2-5 layers of graphene. Clear lattice fringes are observed during TEM analysis. The lattice fringe spacing of SiC grain was determined from the images to be 2.5 Å corresponding to the (111) crystal plane of β-SiC, which agrees well with the fast Fourier transformation (FFT) results shown in the figure. Only (111) crystal plane of β-SiC is observed in FFT images which means (111) is the preferential crystal orientation as shown by XRD results. Meanwhile, the lattice fringe of (002) crystal plane of graphite can be also identified and the lattice fringe spacing was determined to be 3.4 Å. The (002) crystal plane of graphite is identified to be the preferential crystal orientation in the FFT image of graphite phase which agrees well with XRD results. The curve and fracture of graphite phase leading to the high intensity of D band in Raman analysis is observed in TEM images.

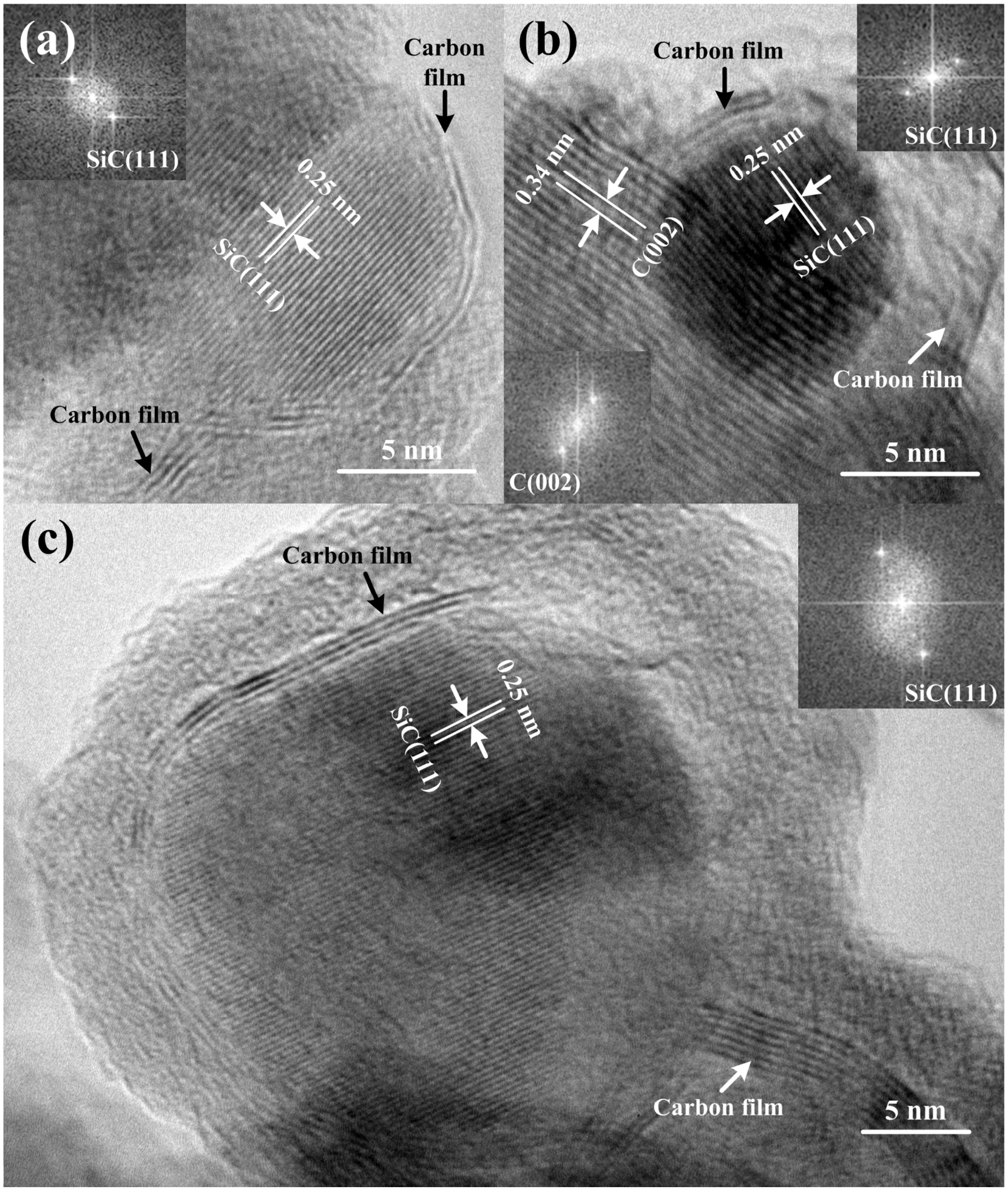

Fig. 5 Typical bright field TEM graphs with FFT images of samples at $SiCl_4$ input rate of (a),(b) 0.42 mol h^{-1}; (c) 0.53 mol h^{-1}.

Surface chemical composition of the samples was analyzed by X-ray photoelectron spectroscopy (XPS). The surface of the sample consists of Si, C, O and Cl indicated by the survey XPS spectrum in Fig. 6 (a). The distinct peaks at around 101.82 eV, 284.80 eV, 532.59 eV and

200.42 eV correspond to Si 2p, C 1s, O 1s and Cl 2p, respectively. Chemical states of the surface elements was further analyzed by high-resolution XPS spectra. Moreover, the deconvolution of the spectra of Si 2p and C 1s was carried out. The Si 2p spectrum can be fitted into 3 peaks at 101.33 eV, 101.75 eV and 103.07 eV corresponding to Si from SiC[39], Si from SiO_2[40] and Si from $(-Si(CH_3)_2O-)_n$[41], respectively. The C 1s spectrum can also be fitted into peaks at 287.42 eV, 287.82 eV and 285.92 eV corresponding to C from SiC[42], C from graphite[43] and C from the carbon network, respectively.[44] O comes from the oxidation of the sample surface. During thermal plasma deposition, dangling bonds like Si-Cl, Si-H and $Si-CH_3$ are formed on the surface. These active bonds can be easily oxidized when contacting with air, leading to the formation of Si-O on the surface. Cl comes from the remaining dangling bonds on the surface which contains Cl atoms.

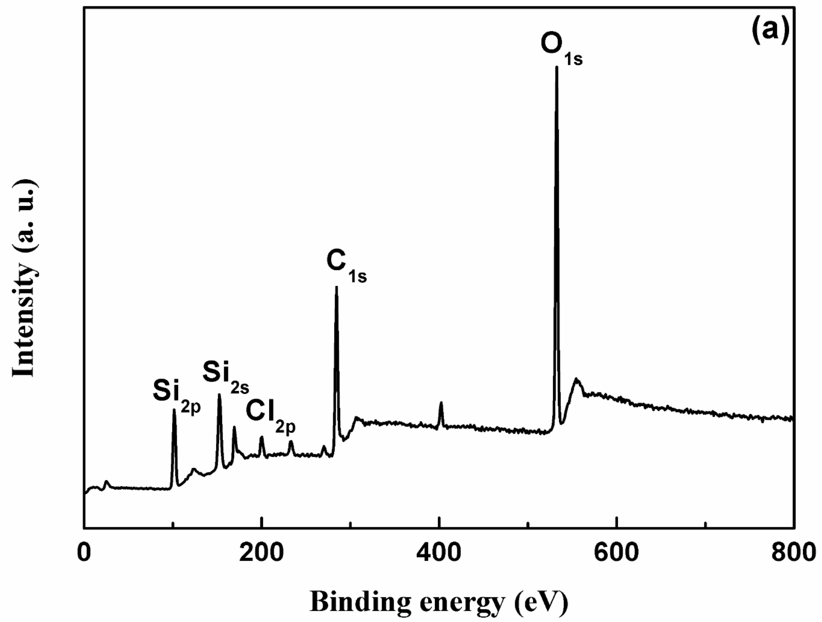

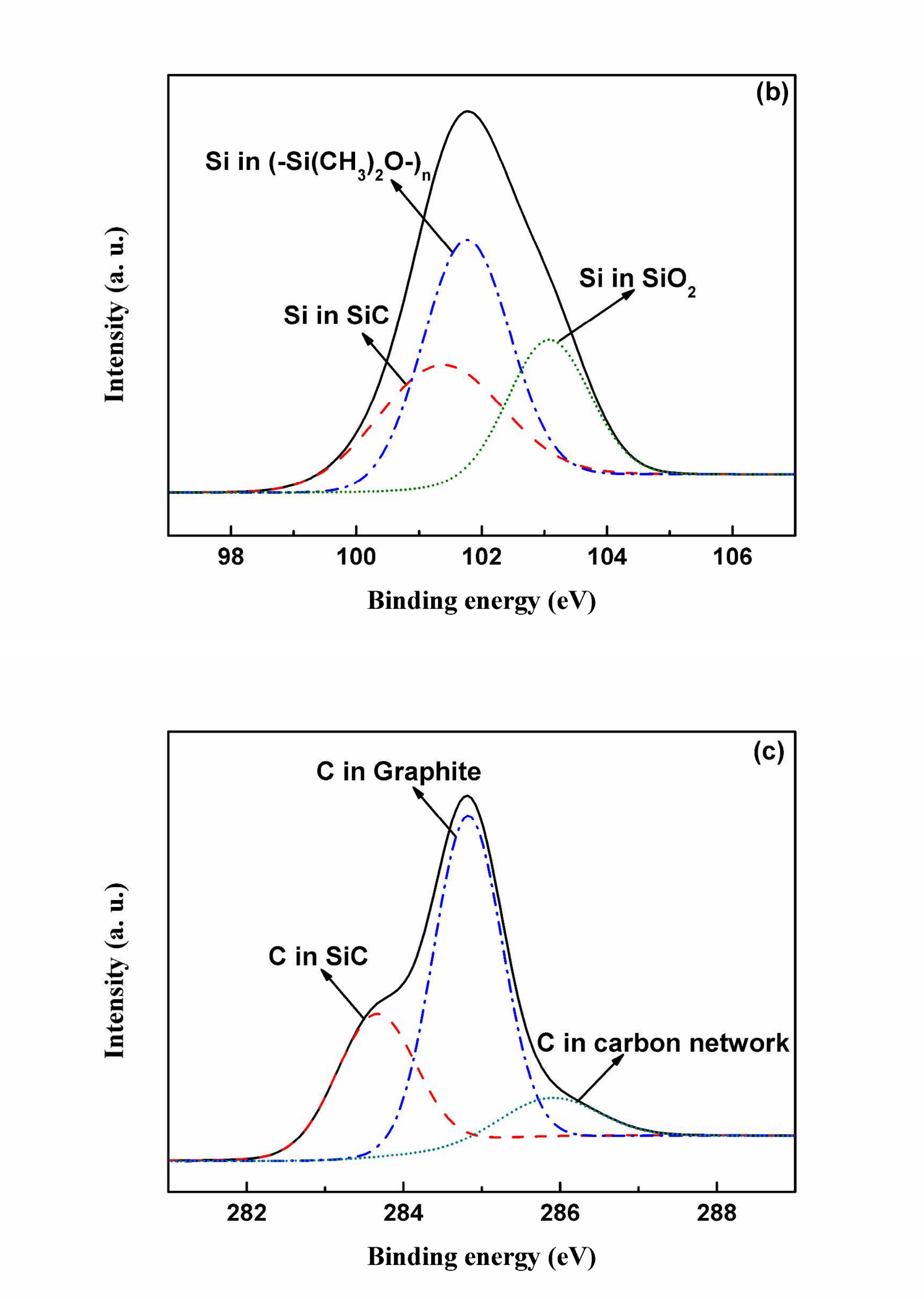

Fig. 6 (a) Survey XPS spectrum of sample deposited at $SiCl_4$ input rate of 0.21 mol h^{-1} and spectra of (b) Si 2p and (c) C 1s.

The C atomic fraction of the samples, defined as the relative atomic fraction of C divided by the combined fraction of Si and C, was computed based on the analysis of the survey XPS spectrum. These results are summarized in Fig. 7 (a). The C atomic fraction of the samples decreases with increasing $SiCl_4$ input rate. Moreover, the mole fraction of SiC, defined as the relative mole concentration of Si from SiC divided by the combined mole concentration of Si from SiC, $(-Si(CH_3)_2O-)_n$ and SiO_2, was calculated from the analysis of the XPS spectrum of Si 2p. The SiC mole fraction first improves and then decreases with increasing $SiCl_4$ input rate which can be seen from Fig. 7 (b). The SiC mole fraction reaches a maximum at $SiCl_4$ input rate of 0.21 mol h^{-1} which means the most SiC component was obtained under this condition.

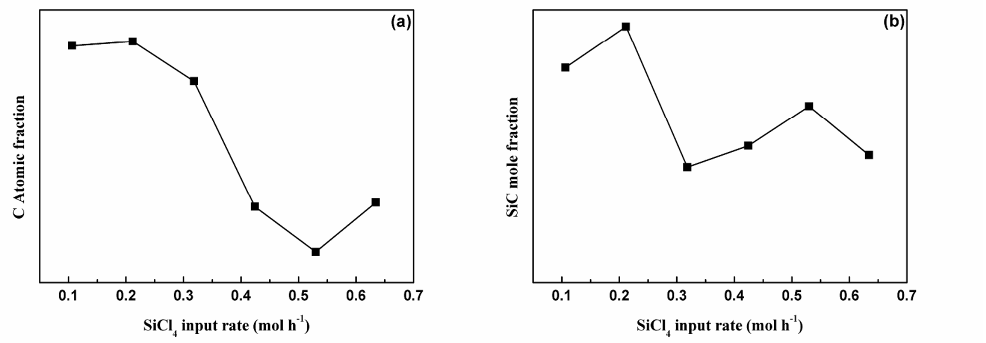

Fig. 7 Effect of $SiCl_4$ input rate on (a) C atomic fraction and (b) SiC mole fraction of samples.

To better understand the effect of $SiCl_4$ input rate on the deposition process and product properties, OES diagnostic of the thermal plasma enhanced deposition was carried out. A typical optical emission spectrum of the thermal plasma deposition at $SiCl_4$ input rate of 0.42 mol h^{-1} is shown in Fig. 8. Excited species like Si^*, C^*, H^* and Ar^* are observed and marked in the images, which indicates the sufficient ability of thermal plasma to decompose $SiCl_4$, CH_4 and H_2 into atomic state. The effect of $SiCl_4$ input rate on three emission lines was studied, which located at 288.17 nm, 247.83 nm and 656.24 nm corresponding with Si^*, C^* and H^*, respectively. As can be seen from Fig. 9, the emission intensity of Si (288.17 nm) improves with $SiCl_4$ input rate and gets to a platform when $SiCl_4$ input rate reaches 0.42 mol h^{-1}. In this thermal plasma deposition system, the effect of precursors input on the electron density of the plasma can be negligible and thus the emission intensity of Si^* and C^* linearly correlates with the concentration of atomic Si and C in the gas phase, respectively.[33] Therefore, the increase of $SiCl_4$ input rate enhances the concentration of atomic Si in the gas phase while the concentration of atomic C first improves and then decreases depending on the OES diagnostic results in Fig. 9. The concentrations of atomic Si and C in the gas phase are found to be the main factors affecting the deposition process and product properties. Higher atomic Si concentration in the gas phase leads to more Si deposited in the sample, resulting in the increase of thin film deposition rate and the decrease of C atomic fraction. More SiC will be formed with more atomic Si and C in the gas phase when first increasing $SiCl_4$ input rate. However, the amount of atomic C then turns to be insufficient and the redundant Si prefers to form a-Si rather than SiC, leading to the decrease of SiC mole fraction at higher $SiCl_4$ input rate.

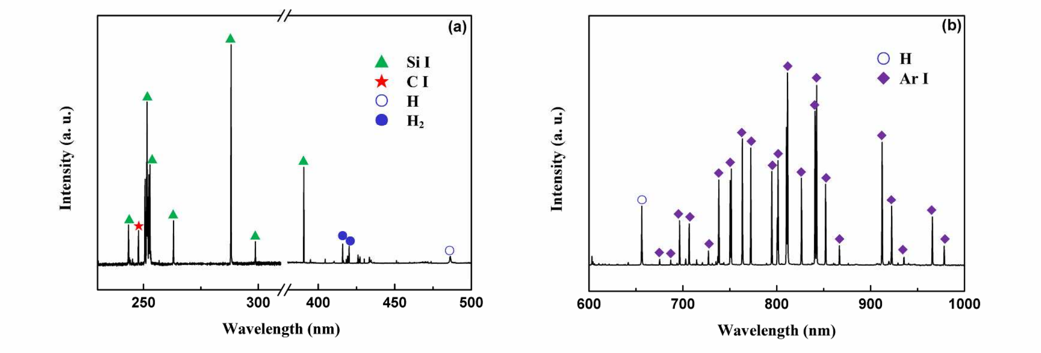

Fig. 8 Typical optical emission spectrum of thermal plasma deposition at $SiCl_4$ input rate of 0.42 mol h^{-1} in the wavelength of (a) 200-500 nm and (b) 600-100 nm.

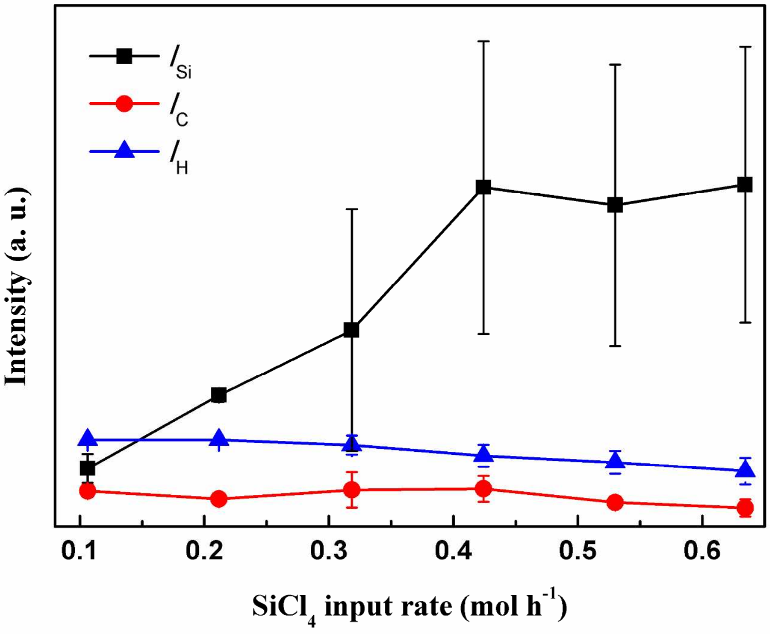

Fig. 9 Effect of $SiCl_4$ input rate on the emission intensities of Si (288.17 nm), C (247.83 nm) and H (656.24 nm).

Based on the characterization and OES diagnostic results summarized above, the deposition mechanism in the APTPECVD process was simply deduced and shown in Fig. 10. Si source ($SiCl_4$) and C source (CH_4) together with H_2 are imported into thermal plasma where these precursors are decomposed into atomic Si, C, H and Cl through Eqs. (2)-(4).

$$SiCl_4 + M \rightarrow Si + 4Cl + M, \text{ (M represents } e^- \text{ or Ar)} \tag{2}$$

$$CH_4 + M \rightarrow C + 4H + M, \tag{3}$$

$H_2 + M \rightarrow 2H + M.$ (4)

When these excited species flow to a low temperature zone, combination between these species begins, leading to the formation of small molecules, such as HCl and chlorosilanes, and crystal nucleus through Eqs. (5)-(8).

$H + Cl \rightarrow HCl,$ (5)

$Si + xH + (4-x)Cl \rightarrow SiH_xCl_{4-x}, (x = 0, 1, 2, 3)$ (6)

$Si + C \rightarrow SiC(s),$ (7)

$C \rightarrow C(s).$ (8)

The crystal nucleus grows through collision when they continue to travel in the plasma to places at a lower temperature. As the input rate of CH_4 is higher than $SiCl_4$, more C related species are formed in the plasma. C is found not only in SiC but also in graphite. Small molecules and clusters prefer to attach on particles previously formed in the plasma, such as SiC nanocystals. Finally, these particles leave the plasma and deposit on the substrate to form thin film samples. These result in the morphology observed in Fig. 5, i.e., SiC nanocrystals are covered by carbon films and embedded in the network formed by graphite and a-Si, and explain the appearance of dangling bonds on the surface of the sample.

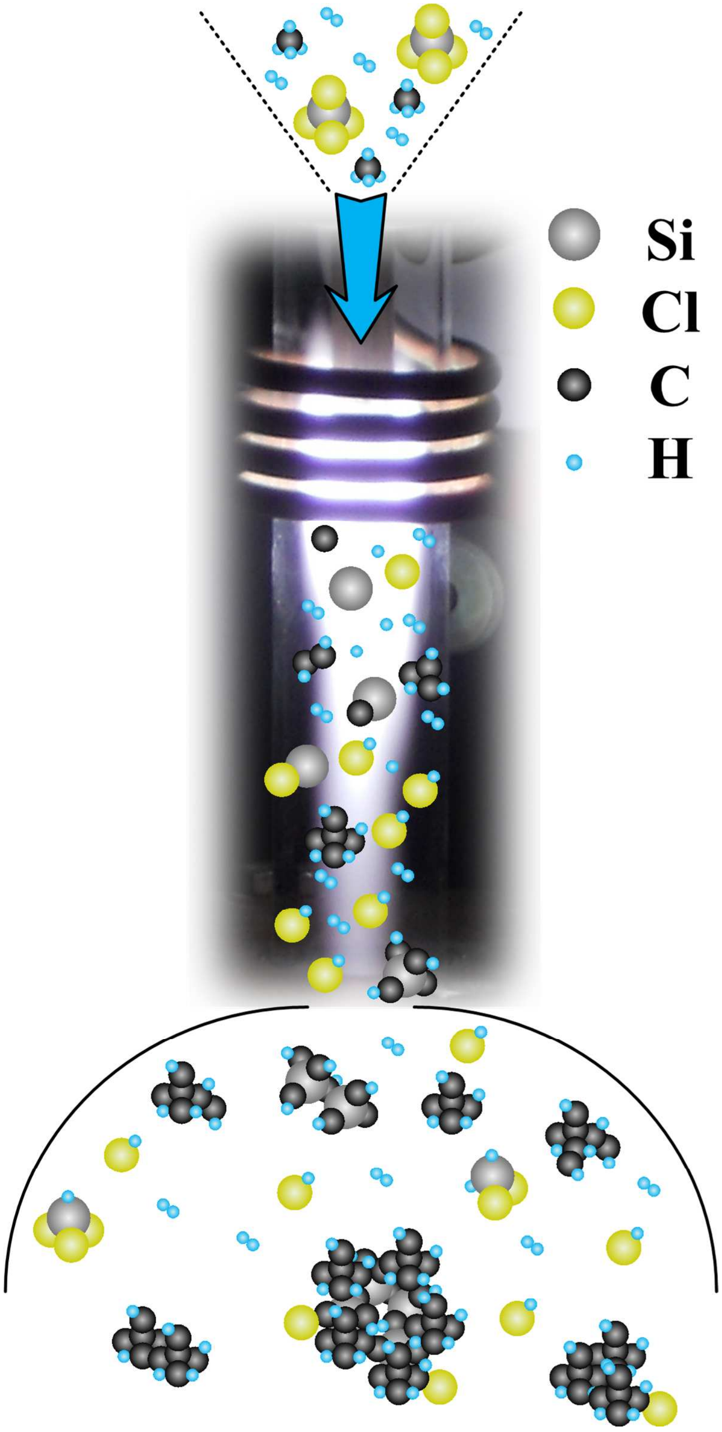

Fig. 10 Schematic diagram of the deposition mechanism of APTPECVD process.

Experimental

Fabrication of SiC nanocrystals

The APTPECVD apparatus with OES diagnostic equipment has been discussed elsewhere.[29, 33] The thermal plasma is generated by a RF plasma source with a power up to 10 kW. $SiCl_4$ and CH_4 diluted by H_2 are used as Si and C sources, respectively. Ar is the plasma working gas. The input rate of $SiCl_4$ is changed from 0.11 to 0.63 mol h^{-1} to study the effect of $SiCl_4$ input rate on the deposition process while the input rate of CH_4 and H_2 is fixed at 0.51 and 1.54 mol h^{-1}. The volatile $SiCl_4$ precursor is transferred into a plastic injector in the fuming cupboard and pumped into the deposition system using an injection pump. Both crystalline silicon and glass are used as substrates.

Characterization

The morphology and nanostructure of the samples are characterized using a scanning electron microscope (SEM, JSM-6460LV) and a transmission electron microscope (HRTEM, JEM-2010). The crystal structure of the sample is analyzed by X-ray diffraction (XRD, Bruker D8 Advance) with monochromatized Cu Kα radiation between scattering angles of 5° and 90° and a micro Raman spectroscope (Horibra LABRAM-HR) with 532 nm He–Ne laser excitation between wavelength of 300 and 3000 cm^{-1}. The surface elemental composition of the samples is analyzed by X-ray photoelectron spectroscopy (XPS, ESCALAB 250Xi) with Al Kα radiation and the C1s peak at 284.6 eV as an internal standard.

Conclusion

SiC nanocrystal is a promising material with potential applications in electronic, photovoltaic and biological fields. In this work, SiC nanocrystal was fabricated using an APTPECVD process with $SiCl_4$ as Si source and CH_4 as C source. The thermal plasma enhanced CVD process and product properties were thoroughly studied. The SiC nanocrystals produced are covered by carbon films and embedded in the network formed by graphite and a-Si. The deposition rate of the thin film improved with increasing $SiCl_4$ input rate and reached a maximum of ~70 nm s^{-1}. The SiC nanocrystal has an average grain diameter in the range of 21-33 nm. Effect of $SiCl_4$ input rate on the surface chemical composition of the samples was studied, and the C atomic fraction and SiC mole fraction of the samples were calculated. OES diagnostic was carried out to better understand the effect of $SiCl_4$ input rate on the deposition process. The concentrations of atomic Si and C in the gas phase were found to be the main factors affecting deposition rate and product properties. Based on these experimental results, a simple deposition mechanism in the APTPECVD process was deduced, indicating that SiC nanocrystal is formed by the assembly of atomic species formed by thermal plasma decomposition of Si and C precursors.

Acknowledgements

This study is supported by the National Basic Research Program of China (973 Program no. 2012CB720301), the National Natural Science Foundation of China (NSFC) under grant no. 21176137. We are also grateful for Mr. Zezhong Cao's help on the deposition experiments.

References:

1. D. Nakamura, I. Gunjishima, S. Yamaguchi, T. Ito, A. Okamoto, H. Kondo, S. Onda and K. Takatori, *Nature*, 2004, **430**, 1009-1012.
2. P. Melinon, B. Masenelli, F. Tournus and A. Perez, *Nat. Mater.*, 2007, **6**, 479-490.
3. C. R. Eddy and D. K. Gaskill, *Science*, 2009, **324**, 1398-1400.
4. S. Castelletto, B. C. Johnson, V. Ivady, N. Stavrias, T. Umeda, A. Gali and T. Ohshima, *Nat. Mater.*, 2014, **13**, 151-156.
5. P. Aspenberg, A. Anttila, Y. T. Konttinen, R. Lappalainen, S. B. Goodman, L. Nordsletten and S. Santavirta, *Biomaterials*, 1996, **17**, 807-812.
6. T. Matsumoto, J. Takahashi, T. Tamaki, T. Futagi, H. Mimura and Y. Kanemitsu, *Appl. Phys. Lett.*, 1994, **64**, 226-228.
7. J. S. Shor, L. Bemis, A. D. Kurtz, I. Grimberg, B. Z. Weiss, M. F. Macmillian and W. J. Choyke, *J. Appl. Phys.*, 1994, **76**, 4045-4049.
8. Y. P. Guo, J. C. Zheng, A. Wee, C. Huan, K. Li, J. S. Pan, Z. C. Feng and S. J. Chua, *Chem. Phys. Lett.*, 2001, **339**, 319-322.
9. J. Zhu, Z. Liu, X. L. Wu, L. L. Xu, W. C. Zhang and P. K. Chu, *Nanotechnology*, 2007, **18**.
10. D. J. Dai, N. Zhang, W. X. Zhang and J. Y. Fan, *Nanoscale*, 2012, **4**, 3044-3046.
11. J. Y. Fan, H. X. Li, J. Iiang, L. So, Y. W. Lam and P. K. Chu, *Small*, 2008, **4**, 1058-1062.
12. J. Y. Fan and P. K. Chu, *Small*, 2010, **6**, 2080-2098.
13. B. Somogyi, V. Zolyomi and A. Gali, *Nanoscale*, 2012, **4**, 7720-7726.
14. D. Beke, Z. Szekrenyes, D. Palfi, G. Rona, I. Balogh, P. A. Maak, G. Katona, Z. Czigany, K. Kamaras, B. Rozsa, L. Buday, B. Vertessy and A. Gali, *J. Mater. Res.*, 2013, **28**, 205-209.
15. J. S. Shor, I. Grimberg, B. Z. Weiss and A. D. Kurtz, *Appl. Phys. Lett.*, 1993, **62**, 2836-2838.
16. D. Beke, Z. Szekrenyes, I. Balogh, M. Veres, E. Fazakas, L. K. Varga, K. Kamaras, Z. Czigany and A. Gali, *Appl. Phys. Lett.*, 2011, **99**.
17. Y. Li, C. X. Chen, J. T. Li, Y. Yang and Z. M. Lin, *Nanoscale Res. Lett.*, 2011, **6**.
18. S. Askari, I. Levchenko, K. Ostrikov, P. Maguire and D. Mariotti, *Appl. Phys. Lett.*, 2014, **104**, 163103-163105.
19. Q. Cheng, E. Tam, S. Xu and K. K. Ostrikov, *Nanoscale*, 2010, **2**, 594-600.
20. K. K. Ostrikov, D. H. Seo, H. Mehdipour, Q. Cheng and S. Kumar, *Nanoscale*, 2012, **4**, 1497-1508.
21. T. Takeshita, K. Ichige, Y. Kurata and S. Hasegawa, *J. Appl. Phys.*, 1991, **69**, 7945-7947.
22. M. I. Chaudhry and R. L. Wright, *Appl. Phys. Lett.*, 1991, **59**, 51-53.
23. K. L. Cheng, H. C. Cheng, W. H. Lee, C. P. Lee, C. C. Liu and T. R. Yew, *Appl. Phys. Lett.*, 1997, **70**, 223-225.
24. Y. Sun, T. Miyasato, J. K. Wigmore, N. Sonoda and Y. Watari, *J. Appl. Phys.*, 1997, **82**, 2334-2341.
25. S. Kerdiles, R. Rizk, A. Perez-Rodriguez, B. Garrido, O. Gonzalez-Varon, L. Calvo-Barrio and J. R. Morante, *Solid State Electron.*, 1998, **42**, 2315-2320.
26. S. Kerdiles, A. Berthelot, F. Gourbilleau and R. Rizk, *Appl. Phys. Lett.*, 2000, **76**, 2373-2375.
27. T. Rajagopalan, X. Wang, B. Lahlouh, C. Ramkumar, P. Dutta and S. Gangopadhyay, *J. Appl. Phys.*, 2003, **94**, 5252-5260.
28. H. Colder, R. Rizk, M. Morales, P. Marie, J. Vicens and I. Vickridge, *J. Appl. Phys.*, 2005, **98**.
29. T. F. Cao, H. B. Zhang, B. H. Yan and Y. Cheng, *RSC Adv.*, 2013, **3**, 20157-20162.
30. K. K. Ostrikov, U. Cvelbar and A. B. Murphy, *J. Phys. D Appl. Phys.*, 2011, **44**.

31. K. K. Ostrikov, E. C. Neyts and M. Meyyappan, *Adv. Phys.*, 2013, **62**, 113-224.

32. P. W. Atkins, T. L. Overton, J. P. Rourke, M. T. Weller and F. A. Armstrong, *Inorganic Chemistry*, 5th edn edn., W. H. Freeman and Company, New York, 2010.

33. T. F. Cao, H. B. Zhang, B. H. Yan, W. Lu and Y. Cheng, *RSC Adv.*, 2014, **4**, 15131-15137.

34. H. Fritzsche, M. Tanielian, C. C. Tsai and P. J. Gaczi, *J. Appl. Phys.*, 1979, **50**, 3366-3369.

35. E. Bustarret, M. A. Hachicha and M. Brunel, *Appl. Phys. Lett.*, 1988, **52**, 1675-1677.

36. F. Tuinstra and J. L. Koenig, *J. Chem. Phys.*, 1970, **53**, 1126.

37. A. C. Ferrari, J. C. Meyer, V. Scardaci, C. Casiraghi, M. Lazzeri, F. Mauri, S. Piscanec, D. Jiang, K. S. Novoselov, S. Roth and A. K. Geim, *Phys. Rev. Lett.*, 2006, **97**.

38. A. C. Ferrari and J. Robertson, *Phys. Rev. B*, 2000, **61**, 14095-14107.

39. T. M. Parrill and Y. W. Chung, *Surf. Sci.*, 1991, **243**, 96-112.

40. A. M. Venezia, R. Bertoncello and G. Deganello, *Surf. Interface Anal.*, 1995, **23**, 239-247.

41. M. Morra, E. Occhiello, R. Marola, F. Garbassi, P. Humphrey and D. Johnson, *J. Colloid Interf. Sci.*, 1990, **137**, 11-24.

42. M. Johansson, A. J. Maxwell, S. M. Gray, P. A. Bruhwiler, D. C. Mancini, L. Johansson and N. Martensson, *Phys. Rev. B*, 1996, **54**, 13472-13475.

43. W. M. Lau, L. J. Huang, I. Bello, Y. M. Yiu and S. T. Lee, *J. Appl. Phys.*, 1994, **75**, 3385-3391.

44. Z. H. Wen, G. H. Lu, S. M. Cui, H. Kim, S. Q. Ci, J. W. Jiang, P. T. Hurley and J. H. Chen, *Nanoscale*, 2014, **6**, 342-351.